



Yielding and post-yielding behavior of FDM parts under compression stress at different strain rates

Silvia Ilaria Scipioni¹ · Francesco Lambiase¹

Received: 21 April 2023 / Accepted: 17 July 2023 / Published online: 25 July 2023
© The Author(s) 2023

Abstract

The present study investigates the compression behavior of components made by material extrusion, also known as fused filament fabrication (FFF) or fused deposition modeling (FDM). An experimental plan was conducted by adopting a high-density fulfillment and varying the material flow. Additional tests were performed by thermomechanical compaction to produce full-density samples. Compression tests were performed at various strain rates ranging between 5×10^{-4} and $5 \times 10^{-1} \text{ s}^{-1}$. Yielding and post-yielding behaviors were analyzed. Morphological analysis was carried out to determine the mesostructural features (interlayer neck and void sizes) and how they behave during the compression test. The results indicated that the principal dimension of the voids ranged between 65 mm and 170 mm depending on the adopted value of the extrusion multiplier. On the other hand, thermomechanical compaction enabled the restriction of the voids of printed samples to 10 mm. The cross-sectioning of samples at different strains indicated the formation of shear banding strain localization. In addition, printed samples behaved like porous media during the compression tests and showed different characteristic regions with different void dimensions. The samples printed at the higher material extrusion showed similar behavior to compacted samples. Post-yielding analysis indicated that strain softening observed on compacted samples was more severe as compared to that observed on printed samples. This behavior is dramatically reduced by decreasing the extrusion multiplier.

Keywords Additive manufacturing · Fused deposition modeling · Mechanical characterization · Post-yielding · Morphology

1 Introduction

Additive manufacturing (AM) is gaining a growing impact on manufacturing industries. Since the earlier adoption for rapid prototyping purposes, AM is progressively extending to other applications such as rapid tooling or highly customized products. This is due to the inherent advantages gained by the adoption of these technologies. These involve extreme design flexibility, a high degree of customization, minimum fixed costs, relatively low-cost machining, extremely short setup time, distributed production, as well as a logistic cost reduction [1–3]. The development of machines with higher accuracy, high-temperature heating chambers, as well as the development of new materials even with functionalized

fillers (techno-polymers such as PEEK field [4–9], PEI field [10–16], PAEK field [17, 18], as well as reinforced plastics field [19–25]), offers new possibilities and solutions to solve manufacturing challenges. However, AM components are still affected by some issues which are strictly connected to the layer-by-layer deposition strategy. Internal porosities, voids, distortion, and surface finishing are an issue that is common to many additive manufacturing processes.

Among AM processes, material extrusion (MatExt) represents the most common process used to produce polymeric components. This is due to the machine's simplicity, easy scalability, great material availability, reduced material cost (especially if compared to polymeric powders used in selective laser sintering), and possibility to embed functionalized fillers for structural purposes (such as glass or carbon fibers) or for achieving electrically conductive material (such as copper or even graphene). However, parts made by the MatExt process strongly suffer from the presence of voids [26] which are due to the viscosity of the material during deposition. Indeed, just after the extrusion, rapidly

✉ Francesco Lambiase
francesco.lambiase@univaq.it

¹ Dept. of Industrial and Information Engineering and Economics, University of L'Aquila, via G. Gronchi 18, Zona, 67100 Industriale di Pile, (AQ), Italy

the viscosity rises as the material enters contact with the underlying layer. This limits the contact interface between overlapping layers [27] and strongly limits the degree of healing [28]. The presence of inner voids, as well as the mechanism of adhesion between the layers, can be better described as a sintering process instead of welding; thus, it leads to mechanical behavior very different from those achieved by plastic components processed through other processes, such as injection molding [29–31]. For semicrystalline materials, this is also due to the kinetics of crystallization which may hinder the healing between adjacent deposited filaments [32].

The aim of the present paper is to investigate the influence of voids on the compressive behavior of polymeric components made by the MatExt process under different quasi-static strain rates. To this end, experimental tests were performed by producing nominally full-density samples and varying the material extrusion flow. In addition, reference samples were produced through thermomechanical compaction for benchmarking purposes. The characteristics of the samples produced under different processing conditions such as the density, dimension of voids, and mechanical behavior were investigated.

2 Materials and methods

2.1 Sample production through the FFF process

The study involved polylactide acid (PLA) provided by Fabrix. Material extrusion (MatExt) was adopted to produce the compression tests. Cylindrical samples of 15 mm in diameter and 15 mm in height were produced. The dimension of the samples was adopted to reduce the typical buckling shown by these samples and at the same time increase the strain rate of the tests. The samples were made using a commercial machine model Ender 6 by Creality. The samples were produced with the flat faces parallel to the building plate (as showed in Fig. 1); thus, the compression tests were performed along the z -direction. The main deposition conditions are summarized in Table 1.

The samples were produced by using different material extrusion multipliers: 96%, 100%, and 104%.

2.2 Sample production through thermomechanical compaction

Compaction tests were performed on 3D printing to further reduce the porosities and achieve full-density samples. To this end, prototypal equipment was developed to conduct compression molding tests. The equipment involved a die (with an inner diameter of 15 mm) and a punch (with the same diameter) made by K720 steel by Bohler. An external

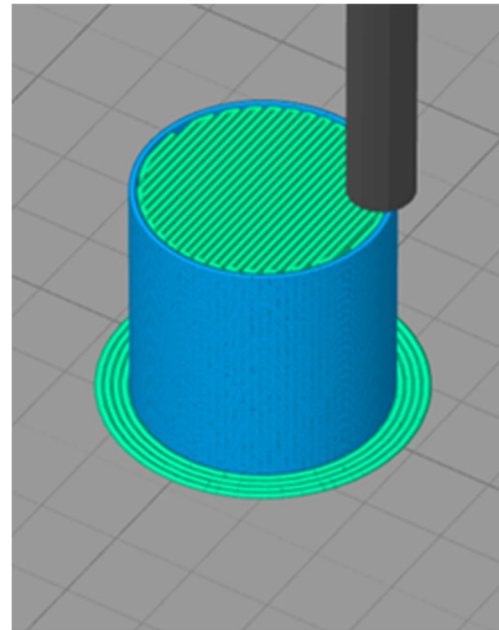


Fig. 1 Schematic of the sample produced with the selected deposition strategy

Table 1 Main deposition conditions

Process parameter	Value
Nozzle temperature (°C)	210
Building plate temperature (°C)	60
Extrusion speed (mm min ⁻¹)	4000
Nozzle diameter (mm)	0.4
Extrusion width (mm)	0.5
Layer thickness (mm)	0.2
Infill percentage (%)	100
Infill strategy	Rectilinear
Number of external shells	1

heater and a K-type thermocouple were used to heat the die under controlled temperatures. The heater and the thermocouple were connected to an external PID for temperature control. During the compaction tests, an external compression force was applied through a hydraulic press.

The compaction tests were conducted under a constant temperature of 120 °C and compaction force of 1500 N (corresponding to a pressure of almost 8.5 MPa). A schematic of the adopted equipment and the mechanical and thermal cycles is depicted in Fig. 2.

2.3 Sample characterization

All samples, those produced through MatExt and those made by compression molding, were characterized to determine the

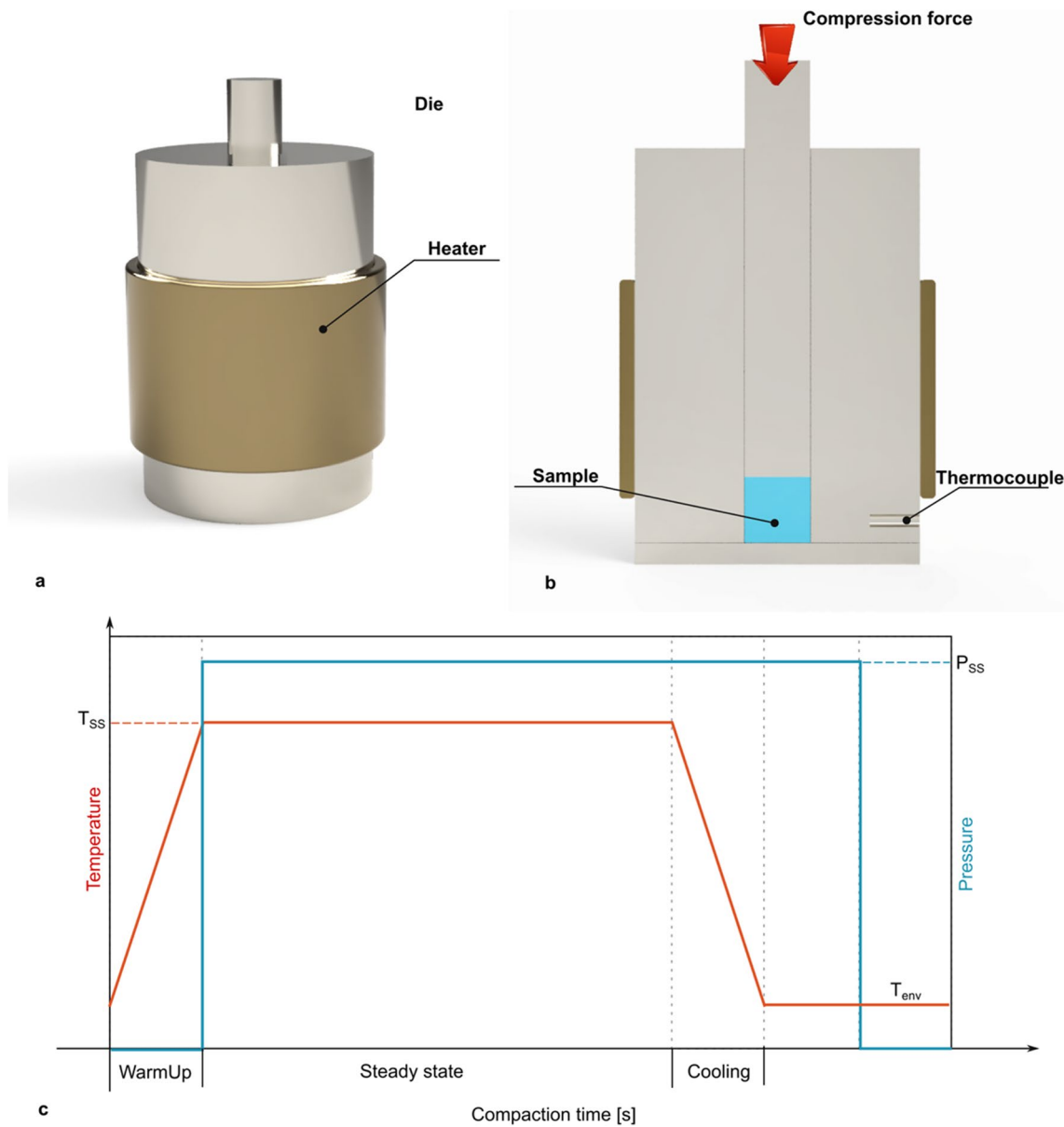


Fig. 2 Schematic of the thermomechanical compaction equipment

density of the components. To this end, the dimensions were measured through a centesimal micrometer. Then, the weight of the samples was measured through a balance model XT1220M by Precisa. This enabled the estimation of the density of the samples and how it was influenced by the adopted process parameters. Compression tests were performed according to ASTM D695 standards. A universal testing machine mode C43.50 equipped with a load cell with a full scale of 50 kN was adopted. The tests were conducted under different strain rates ranging between 5×10^{-4} and $5 \times 10^{-1} \text{ s}^{-1}$.

For each deposition condition and testing condition, five replicates were performed. The final experimental plan is summarized in Table 2.

Optical microscopy was adopted to better understand the morphology of the samples before and after the mechanical tests. To this end, a stereoscope model M205 by LEICA was adopted to determine the morphology of

Table 2 Levels of the full factorial experimental plan

Level	Extrusion multiplier (%)	Strain rate (s^{-1})
I	96	5×10^{-1}
II	100	5×10^{-2}
III	104	5×10^{-3}
IV	Compaction	5×10^{-4}

the upper surface. In addition, a metallographic microscope model DM5000 by LEICA was adopted to provide a better understanding of the mesostructural features (inter-layer neck and void sizes). To better observe the inner defects of the samples, and the influence of the material flow, some samples were cross-sectioned and polished using abrasive paper (up to 2400 grit). To this end, the samples were previously cross-sectioned using a cooled diamond blade. Then, the samples were molded and polished according to the standard metallographic procedures.

3 Results

3.1 Physical characteristics of the samples

Figure 3 compares the densities of the samples produced with different extrusion multipliers (EMs) and those of

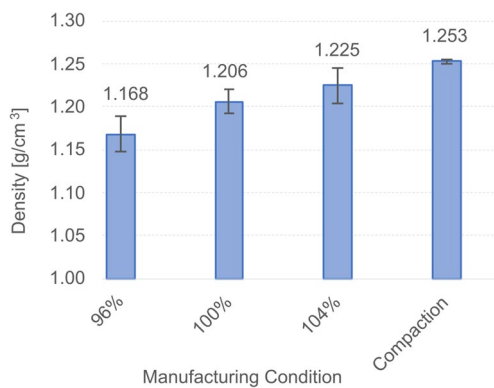


Fig. 3 Influence of the extrusion multiplier (in FFF) and thermomechanical compaction on the density of the samples

samples produced through thermomechanical compaction. As can be inferred, increasing EM from 96 to 100% leads to an increase from 1.17 to 1.21 g cm⁻³ (corresponding to 4% of the increase), while further increase leads to a minor increase in density of almost 2%. This density-saturation phenomenon was already observed in previous studies [26, 33]. The comparison of the density achieved when using the highest extrusion multiplier (EM = 104%) and the thermo-mechanical compaction indicates that the adoption of EM = 104% leads to a slightly lower density (almost 2% lower) as compared to thermomechanical compacted samples. In addition, the mean value of the density achieved by compacted samples corresponds to the density of the PLA reported by the filament manufacturer (1.25 g cm⁻³). This indicates that the developed compaction process enabled to removal of almost all voids from the samples made by MatExt.

To better analyze the influence of the manufacturing conditions on the density of the samples, optical microscopy and SEM analysis were adopted to observe the cross sections of the samples. Figures 4 and 5 show the cross sections of the samples made under different processing conditions.

Image analysis was performed to determine the porosity dimensions produced under different processing conditions. Figure 6 depicts void detection and statistical dimension characterization using a cross-sectional image of a sample produced with an extrusion multiplier of 96%. Starting from an image of the cross section (Fig. 6a), the software determines the presence of voids that are subsequently identified through different colors (Fig. 6b). Then, the dimension of the voids is determined as shown in Fig. 6c, d. The same procedure was followed to analyze the cross section of samples produced under different conditions (i.e., different extrusion multipliers and material extrusion/compaction process).

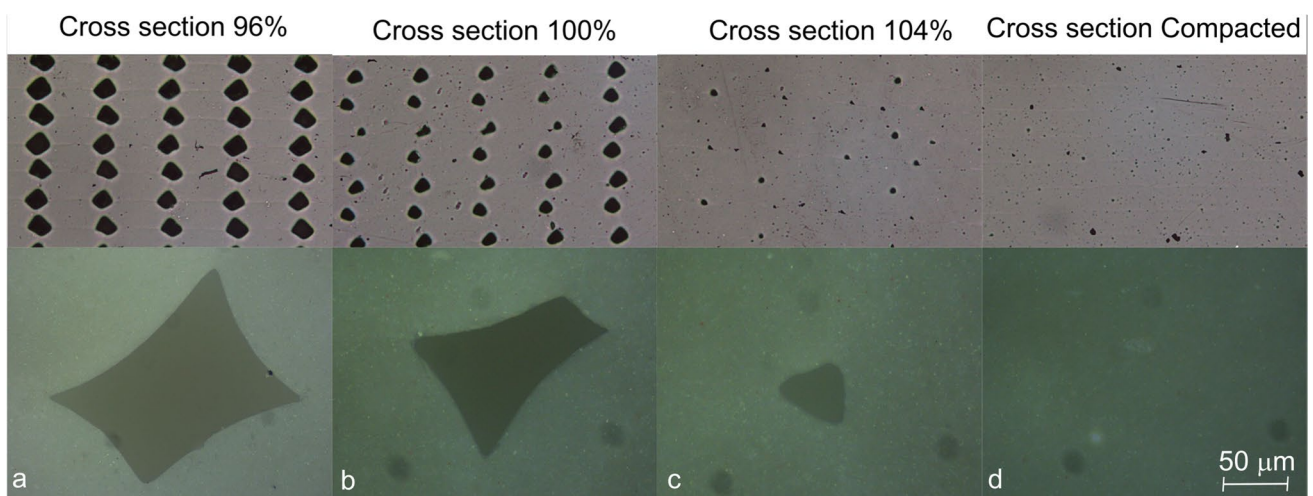


Fig. 4 Cross sections of the samples produced under different processing conditions: **a** EM = 96%, **b** EM = 100%, **c** EM = 104%, and **d** compacted

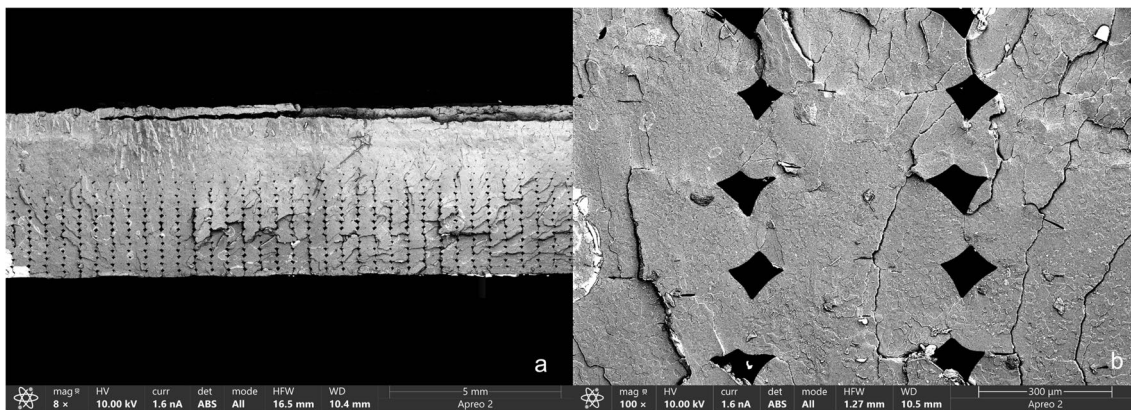
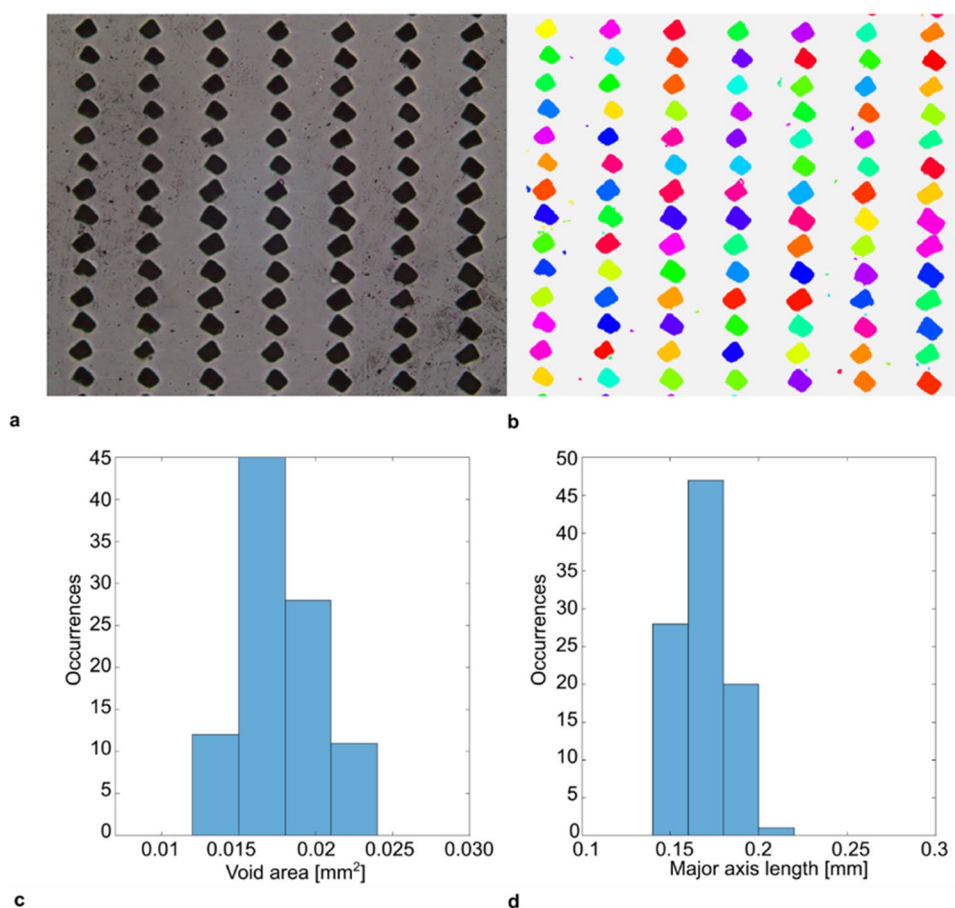


Fig. 5 Cross section of the samples made by SEM analysis at 8× magnification (a) and 100× magnification (b)

Fig. 6 Image analysis of mesostructure features (voids): a original image, b identified voids, c distribution of void area, and d distribution of major axis length. (Extrusion multiplier (EM) = 96%)



When the extruder multiplier was set to 96%, the normal value of the major axis dimension was 170 μm. This value decreased to 125 μm (for EM = 100%) and to 65 μm (for EM = 104%). The voids almost disappeared for the compacted samples (the porosity with the highest major axis dimension was 20 μm). Similarly, the normal void area was determined for each condition. For EM = 96%, the normal

value of the void area was 0.015 mm². This decreased to 0.01 mm² for EM = 100% and further reduced to 0.0025 mm² for EM = 104%. The influence of the deposition conditions (and the adopted process) on the normal value of the characteristic dimension of the voids is depicted in Fig. 7.

These results indicate that increasing EM involved significant reduction of the dimensions of inner voids.

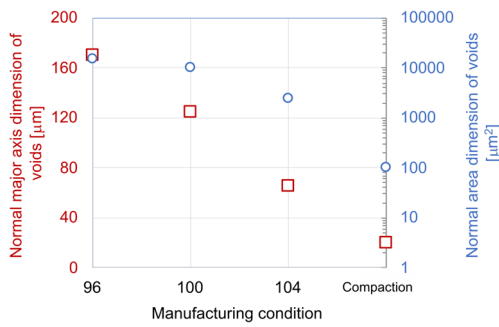


Fig. 7 Normal dimensions of voids produced under different deposition conditions and compaction

Table 3 Density and relative densities calculated according to different manufacturing conditions

Manufacturing condition	Density (g cm^{-3})	Relative density (%)
96%	1.17	93%
100%	1.21	96%
104%	1.23	98%
Compaction	1.25	100%

Increasing EM from 96 to 104% reduced the voids area to one-sixth from $15,000 \text{ mm}^2$ (for EM = 96%) to 2500 mm^2 (for EM = 104%).

Both the cross sections and the quantitative measurement of voids indicated that thermomechanical compaction allowed to fulfill the inner voids almost completely. Thus, the density of these samples was assumed as that of a real full density sample. Thus, the relative density ρ_R calculated by normalizing the density of the sample ρ_S by that of the full density sample (ρ_{FD}) was calculated for all conditions, according to Eq. 1:

$$\rho_R = \frac{\rho_S}{\rho_{FD}} \quad (1)$$

The values of the relative densities of the samples produced using different extrusion multiplier are reported in Table 3.

Morphological analysis was also conducted on the samples to determine possible influence of the processing conditions on the surface appearance. Figure 8 shows the external surfaces of the samples made under different processing conditions and produced by MatExt and compaction tests.

The surfaces were subsequently analyzed using LEICA Map software for 3D reconstruction and analysis. Figure 9a depicts the geometry of a sample produced with by MatExt setting the extrusion multiplier to 104%, while Fig. 9b shows the surface of the compacted samples. As can be inferred, the sample produced through MatExt process shows typical features given by layer-by-layer deposition. On the other hand, the sample made by compaction shows a smoother geometry, as also shown in the virtual cross section, depicted in Fig. 9d. This further indicates that the compaction experiments enabled to produce sufficient material flow to remove the mesoscale features (owing to the previous MatExt process) almost completely.

3.2 Mechanical behavior of the samples

Figure 10 shows a macrograph of a sample used in compression tests before and after the mechanical test. As can be observed, after the tests, the sample shows a barreling effect on the sides. This was achieved for all the samples irrespective of the processing conditions or the manufacturing process (MatExt or compaction).

The typical engineering stress-strain curve is depicted in Fig. 11. The engineering stress was calculated as the ratio of the load by the initial sample diameter, and engineering strain was calculated as the ratio of the deformation by the initial sample height. The curve showed typical characteristics of compression tests on polymers [34, 35]. Indeed, they showed an elastic regime upon the onset of yielding (peak of the stress). Then, post-yielding behavior involving strain

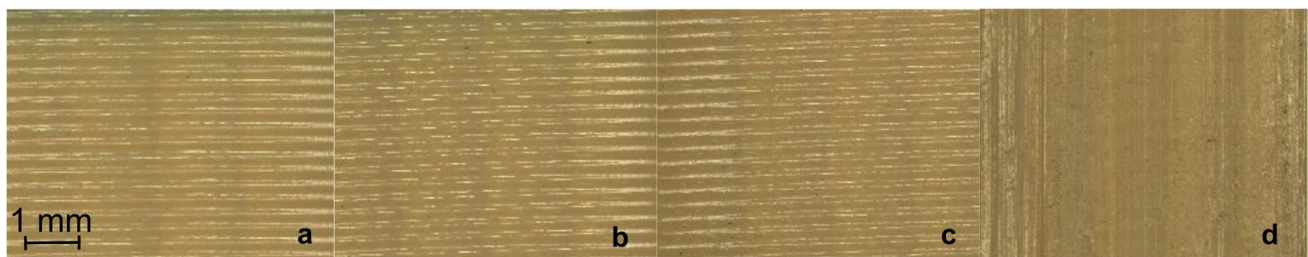


Fig. 8 External surfaces of the samples produced under different processing conditions: **a** EM = 96%, **b** EM = 100%, **c** EM = 104%, and **d** compacted

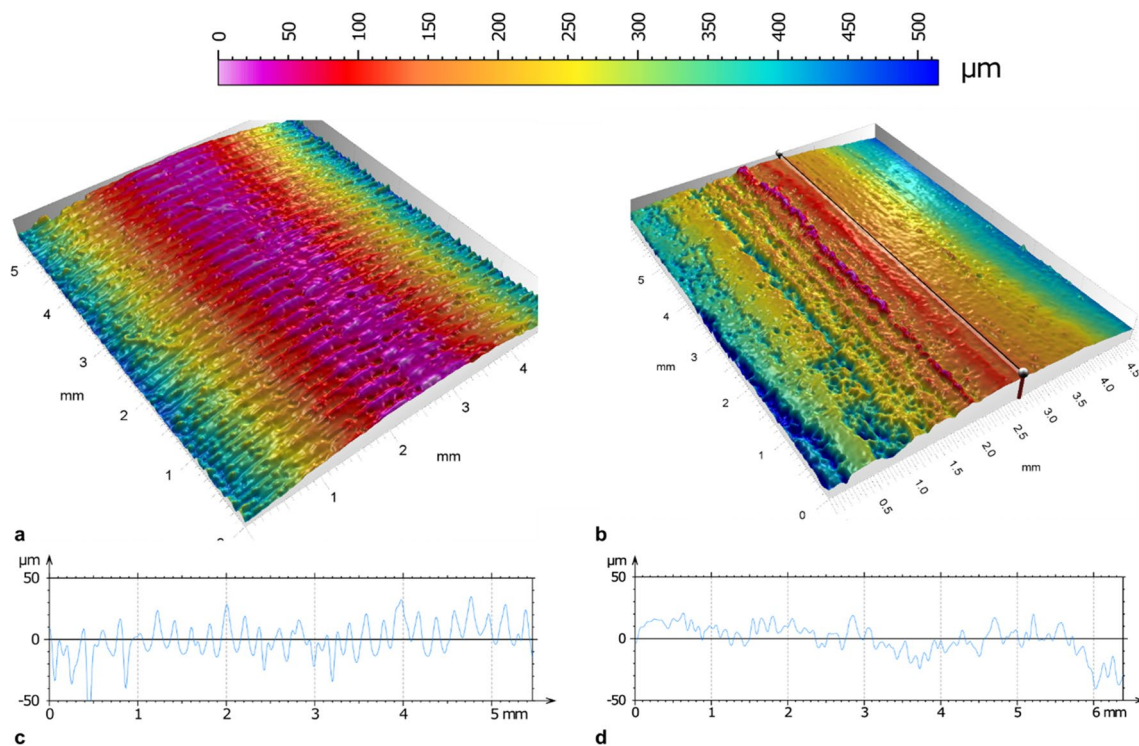


Fig. 9 Surface analysis performed on two samples: **a** printed with extrusion multiplier set to 104% and **b** compacted. Virtual profile of the samples: **c** EM = 104% and **d** compacted.

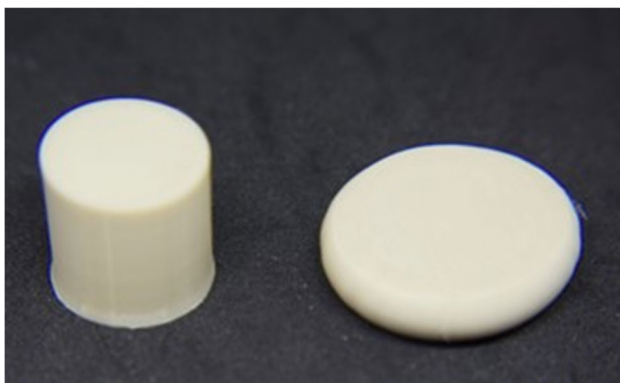


Fig. 10 Macrograph of a sample before and after compression tests

softening (stress drop) was observed. The stress held almost constant (steady state flow) upon the onset of the strain hardening (owing to molecular chains’ alignment towards the loading path).

The influence of the manufacturing process (MAtExt or compaction), the extrusion multiplier, and the strain rate on the yield strength, strain-softening, and strain-hardening behaviors can be retrieved from Fig. 12.

As can be seen, increasing the material extrusion involved higher stress which indicates a higher load-bearing capability of the material. The samples made by the compaction

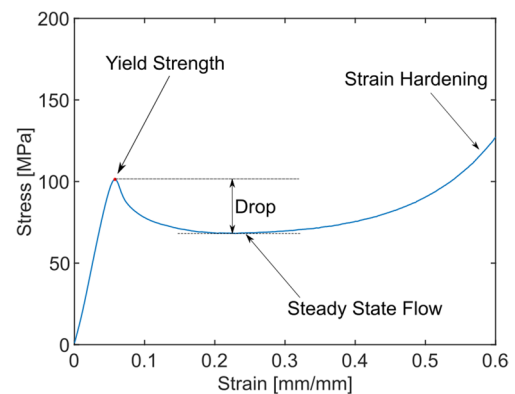
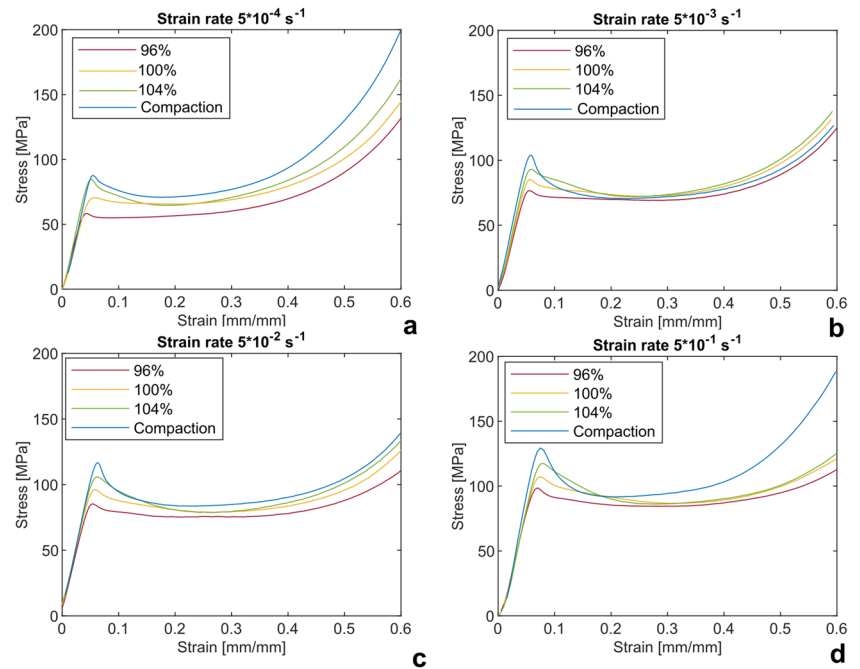


Fig. 11 Stress-strain curves of the samples produced under different processing conditions

process showed the highest yield strength irrespective of the strain rate. This was due to the higher relative density of compacted samples than MAtExt samples. However, a partial contribution was also provided by the aging of the polymer during compaction. The presence of aging was more evident from the analysis of the post-yielding behavior. Indeed, the strain softening behavior was more marked on the compacted samples as compared to MAtExt samples, which were also strongly influenced by the extrusion multiplier. The compacted samples showed a severe strain softening

Fig. 12 Stress-strain curves recorded during the compression tests of the samples produced under different processing conditions (both strain rate and manufacturing process)



with a stress drop from 117 to 85 MPa after yielding (corresponding to 27%). Strain softening is commonly related to the aging of the polymer. Indeed, the thermomechanical compaction was performed at 120 °C. Such temperature is well below the melting temperature of the PLA (almost 175 °C). Thus, the steep drop as well as the narrow deformation involving such a drop indicates the occurrence of polymer aging [36]. MatExt samples showed minor strain softening. These samples did not experience artificial aging owing to the thermal cycle of the compaction. Consequently, the aging was limited to that developed during the MatExt process. These samples showed a smoother reduction of the stress after yielding. Besides, the stress drop in these samples diminished by reducing the material multiplier. As an example, for $EM = 96\%$, the stress reduced from 84 (at yielding) to 77 MPa (corresponding to 8.3%). In these samples ($EM = 96\%$), the strain softening was almost imperceptible. However, if the true stress was plotted, the strain softening would be more marked (since the actual cross-sectional area of the sample is often larger than the initial cross-sectional area).

The influence of the process, processing conditions, and strain rate, on the yielding and post-yielding behavior of the samples recorded during the compression tests, was further investigated by computing the yield strength, the strain softening drop, and the steady state flow, as reported in Fig. 13.

As can be inferred, the compressive yield strength increased with the extrusion multiplier. This was due to the higher density of the samples which showed higher load-bearing capability. In addition, even if the samples produced at 104% did not reach the density of compacted

ones (a difference of 2% was determined, as shown in Fig. 3), they showed close yield strength values as compared to those measured on compacted samples. Increasing the extrusion multiplier led to an increase in mechanical characteristics. The reduction of the dimensions of the void resulted in yield strength, steady-state flow, and strain hardening. However, the steady-state flow increases less than the yield strength; thus, a higher extrusion multiplier led to higher strain softening (post-yielding stress drop). This phenomenon may be due to a porosity distribution that is similar during deformation, irrespective of the value of the extrusion multiplier. The strain-softening drop in the compacted specimens was more localized, and this was due to the aging phenomenon. Indeed, the compaction process involved slow cooling from the steady compaction temperature (120 °C). This also explains why the compacted specimens exhibited higher yield strength and drop at a steady state than the specimens with an extrusion multiplier of 104%, despite having very similar densities. Actually, the compacted specimens underwent thermal cycles at temperatures up to 120 °C.

Higher strain rates involved yield strength and steady-state flow increase. Similarly, the latter showed a lower increase than yield strength. Thus, higher strain rates led to higher strain softening (post-yielding drop) with greater localization of deformation in shear bands. As for strain hardening, this also increases as the strain rate increases. Strain hardening, however, occurs at higher strain values. Increasing the strain rate, therefore, postpones strain hardening. This phenomenon was related to the inversion of curves that occurs after steady-state flow, which leads

Fig. 13 Compressive yield strength of the samples

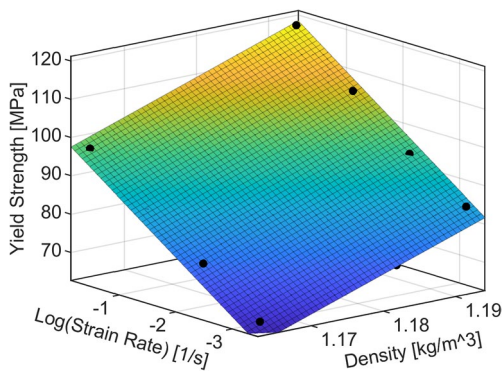
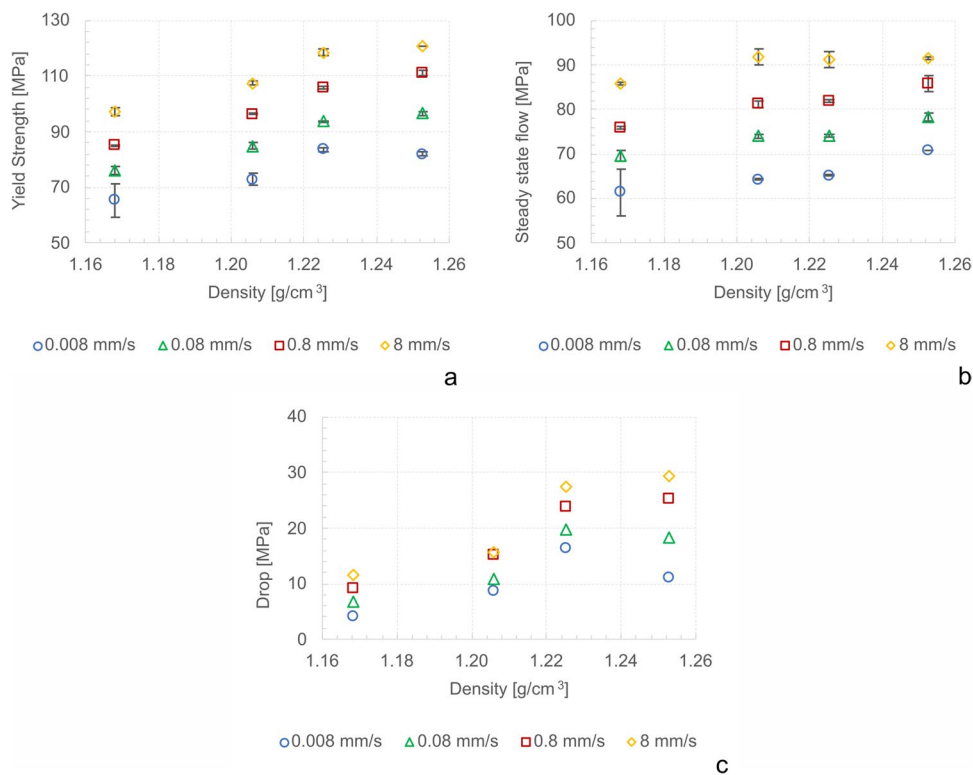


Fig. 14 Empirical model developed to describe the influence of the density of the samples and the strain rate

curves with lower strain rates to grow faster than those with higher strain rates.

An empirical model was developed to describe the influence of the density of the samples and the strain rate. A linear fit model was developed, such as that reported in Fig. 14. The developed model, described by Eq. 2 (where x represents density and y represents $\log(\text{strain rate})$), showed a good fitting with the experimental data since the coefficient of determination R^2 was 0.984 and the adjusted coefficient of determination was 0.9805. Both values were very close to unity indicating a good fitness of the developed model.

$$\sigma_y = -288.4 + 332.7 \cdot \rho + 11.14 \cdot \text{Log}\dot{\epsilon} \tag{2}$$

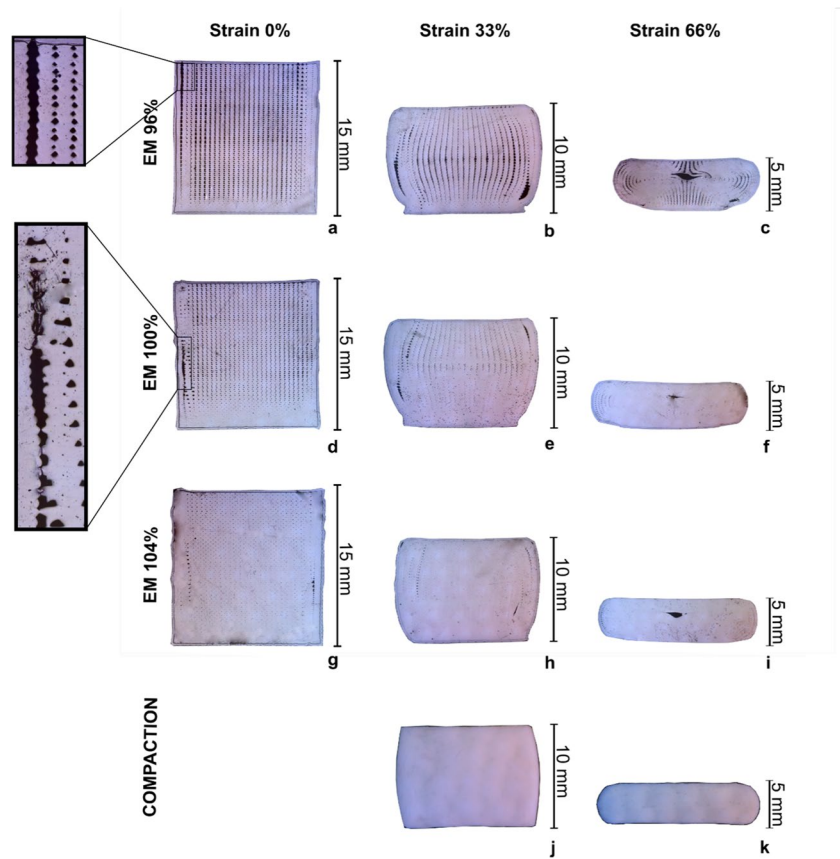
3.3 Analysis of material flow during compression tests

Additional compression tests were performed at intermediate values of the strain to analyze the material flow during the compression tests. To this end, these tests were performed by setting the crosshead displacement value to 10 mm and 5 mm, which led to an engineering strain of 33% and 66%, respectively. These samples were subsequently cross-sectioned to determine the size, shape, and position of the inner voids. Figure 15 shows the cross section of the samples, for each value of the extrusion multiplier. These compression tests were conducted at a strain rate of $5 \times 10^{-2} \text{ s}^{-1}$.

The analysis of the cross sections revealed several issues concerning the deposition distribution. Firstly, poor adhesion between the external skin and the infill layers was observed. This led to larger porosities as can be observed in Fig. 15a (left side) and Fig. 15d (left side). This uneven adhesion led to remarkable skin separation from the infill during deformation, as shown in Fig. 15b, e, and h.

The cross sections of not-compressed samples revealed an uneven distribution of the porosities along the vertical direction. Indeed, the bottom of the samples was characterized by smaller voids. As shown in Fig. 16, this region (in contact

Fig. 15 Cross sections of the samples produced under different manufacturing conditions (96%, 100%, 104%, and compaction) and compressed with different strain (33% and 66%)

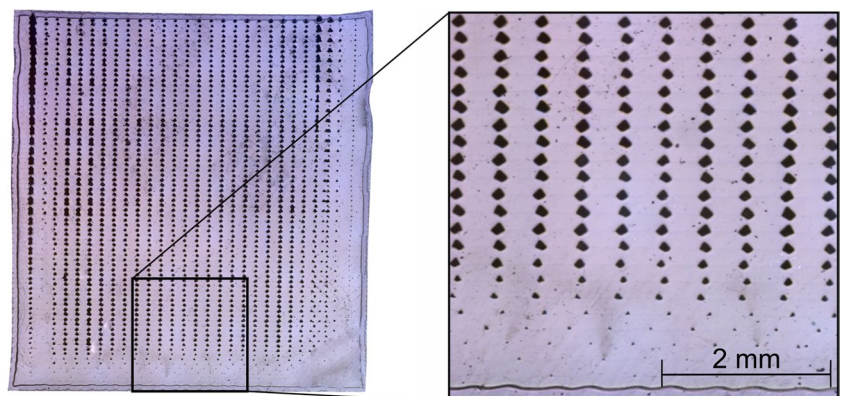


with the building plate) was approximately 1.5 mm in height. Thus, as also reported in [33], this region is more compact than the overlying layers. During the deposition process, the temperature of the building plate was set to 60 °C. Such value was higher than the T_g of the adopted PLA (55 °C). Consequently, the molecular chains within these regions rearranged leading to a much more compact arrangement. During the compression tests, this region showed lower deformation as compared to the overlying layers. Thus, the samples did not show a perfectly barrelling profile, but rather a barrel with a bottom neck. The cross sections of the

samples before compression also reveal significant differences between the different deposition conditions. Indeed, for EM = 96%, many voids were already connected vertically. This defect disappeared almost completely for EM = 100% and EM = 104%.

The distribution of the voids for strain values of 33% and 66% is indicative of the inner deformation within the samples. For relatively low strain (33%), the filaments moved radially (with the exception of the central one). In correspondence with the horizontal symmetry plane, the higher side deformation occurred (since the free edges). At higher

Fig. 16 Higher magnification of a sample printed with EM = 96% showing smaller voids in contact with the building plate



strains, the characteristic regions of compressed samples are clearly visible, namely the shear bands, the dead material zone, and the side regions. During the compression of the samples, the shear bands are a narrow zone where intense plastic deformation occurs. Here, the void dimension was reduced dramatically owing to intense shear strain. In the dead material zone, the region in contact with the compression plates and surrounded by the shear bands reduced strain occurred leading to lower void reduction. Finally, in the side regions, moderate deformation occurred leading to minor void closure. In addition, in the central zone, a macroscopic void resulting from the coalescence of the voids from the dead metal zone is visible.

These four characteristic regions are clearly visible on the samples made with the extrusion multiplier set to 96%, while for higher-density samples, the porosities within the dead material zone are almost imperceptible. In addition, in the specimens made with an extrusion multiplier of 104% and compressed up to a 33% deformation, the only visible voids are those located along the external sides.

Figure 17 depicts the cross section of two samples produced with an extrusion multiplier $EM = 96\%$ after compression performed at different strain rates. The cross sections clearly indicate the great influence of the strain rate on strain localization. Indeed, for a lower strain rate ($5 \times 10^{-4} \text{ s}^{-1}$), a more uniform void distribution was observed (as shown in Fig. 17a). On the other hand, at a higher strain rate ($5 \times 10^{-1} \text{ s}^{-1}$), the deformation was uneven, and the shear bands are clearly visible in Fig. 17b.

4 Discussion

Additive manufacturing processes are rapidly evolving from the initial niche role of rapid prototyping. Today, owing to the significant advantages of these components, the constant development of new materials, as well as the introduction of increasingly precise and repeatable machines, additive manufacturing processes are widely used in rapid tooling and also for the production of secondary structures.

To this end, the ability to predict the mechanical behavior of the components and how this is influenced by the parameters of the printing process is crucial. The aspect that most limit the mechanical characteristics of the components obtained by additive manufacturing is represented

by the internal voids of the components. This is particularly significant in the fused deposition modeling process, due to the high viscosity during the deposition phase. The presence of such voids affects several aspects of a physical nature (e.g., density, thermal conductivity), and of a mechanical nature (stiffness, yield strength, etc.).

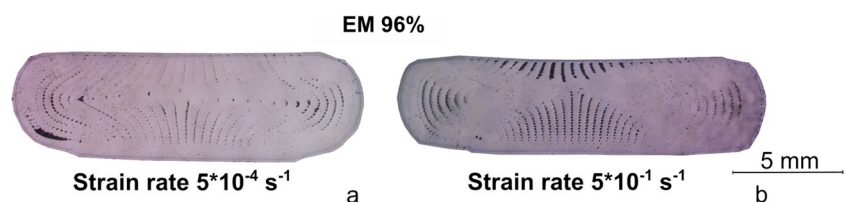
The study is aimed at understanding the relationship between the characteristics of voids and the mechanical behavior of components. To this end, a campaign of experimental tests was conducted through which the relationship between porosity, density, and mechanical characteristics was better deepened. To verify the relationship between density and mechanical characteristics, some specimens were subjected to a thermal compaction process. This process has led to the production of specimens with a density of 1.25 g cm^{-3} , which equals the density of the base material. The thermal compaction process also eliminated the typical layer-by-layer finish present on all MatExt components.

The samples made by MatExt showed characteristics similar to those made by thermal compaction. The yield strength of the specimens was substantially related to the relative density of the component, as confirmed by Eq. 2. However, the characteristics of post-yielding are different. While compacted specimens showed marked strain softening, MatExt specimens are characterized by a lower stress drop. This difference was related to the lowest cooling rate during thermal compaction leading to greater aging of the polymer. Through the realization of compression tests at different deformations and the cross-sectioning, it was possible to qualitatively observe the deformation field. In fact, the samples showed three different regions: (1) shear bands where the deformation localization takes place (and to which strain softening is linked); (2) dead material region—in contact with the compression planes where there are minor deformations; and (3) side region where partial deformation occurs.

The increase in the deformation rate led to an increase in yield strength but also to a greater localization of the deformations and consequently a greater strain softening. To describe the influence of density and strain rate on mechanical characteristics, a linear regression model was developed, which showed a very good fitting, with a correct coefficient of determination R^2 of 0.98.

The results from the optical microscopy of the cross sections indicated the presence of uneven distribution of the

Fig. 17 Effect of the strain rate (during the compression tests) on the distribution of the voids



porosities during the compression tests. In addition, an unexpected formation of a large void in the central region of the samples was observed. This large void was produced through the coalescence of smaller voids which “moved” towards the sample center during compression. To better understand the deformation behavior of MatExt components, a numerical model of the compression test would be beneficial. This represents the next step toward a more comprehensive understanding of the mechanical behavior of such components and will be pursued in next research.

5 Conclusions

This study investigated the influence of the extrusion multiplier on the yielding and post-yielding behavior of MatExt samples under quasi-static compression tests. These tests were conducted under different strain rates ranging between 5×10^{-4} and $5 \times 10^{-1} \text{ s}^{-1}$. Additional samples were produced to achieve a full-density sample through the thermomechanical compression of MatExt samples. A cross-sectional analysis was carried out to better investigate the deformation behavior of the samples during the compression tests. The main achievements of this study are as follows:

- The yield strength of the samples (both made by the MatExt and thermomechanical compaction) can be well predicted by a linear fitting model accounting for the density of the material and the logarithm of the strain rate.
- The density of the samples produced with the extrusion multiplier set to 104% was just 2% lower than the density of thermomechanical compacted samples, which were assumed as real full-density samples.
- The post yielding behavior of the samples was highly influenced by the manufacturing process (MatExt or thermomechanical compaction), the extrusion multiplier, and the strain rate. Thermomechanical compacted samples were characterized by higher strain softening as compared to MatExt samples. This was due to the physical aging of the polymer during the thermomechanical compaction. These samples also showed a narrower region where stress drop developed.
- MatExt samples showed lower softening which reduced with the adopted value of the extrusion multiplier. In samples made with $EM = 96\%$, the stress drop was between 4 MPa and 11.5 MPa (for strain rates of 5×10^{-4} to $5 \times 10^{-1} \text{ s}^{-1}$, respectively) while for $EM = 104\%$, the stress drop was between 16 MPa and 27.4 MPa (for strain rates of 5×10^{-4} to $5 \times 10^{-1} \text{ s}^{-1}$, respectively).
- The cross sections of the samples showed severe strain localization forming shear bands. Such a region of high deformation was characterized by the closure of the voids produced during material extrusion processes. The region

in contact with the compression plates (dead material zone) was still hosting larger voids as well as the side region where lower plastic deformation occurs.

Acknowledgements The authors would like to thank the contribution of Eng. Martina Ficcadenti and Doc. Lorenzo Arrizza for SEM analysis.

Author contribution All the authors contributed to the design and implementation of the research, to the analysis of the results, and to the writing of the manuscript.

Funding Open access funding provided by Università degli Studi dell’Aquila within the CRUI-CARE Agreement.

Data availability Not applicable.

Declarations

Ethical approval Not applicable.

Consent to participate Not applicable.

Consent for publication Not applicable.

Conflict of interest The authors declare no competing interests.

Open Access This article is licensed under a Creative Commons Attribution 4.0 International License, which permits use, sharing, adaptation, distribution and reproduction in any medium or format, as long as you give appropriate credit to the original author(s) and the source, provide a link to the Creative Commons licence, and indicate if changes were made. The images or other third party material in this article are included in the article’s Creative Commons licence, unless indicated otherwise in a credit line to the material. If material is not included in the article’s Creative Commons licence and your intended use is not permitted by statutory regulation or exceeds the permitted use, you will need to obtain permission directly from the copyright holder. To view a copy of this licence, visit <http://creativecommons.org/licenses/by/4.0/>.

References

1. Perez-Mananes R et al (2021) Application of 3D printing and distributed manufacturing during the first-wave of COVID-19 pandemic. Our experience at a third-level university hospital. *3D Print Med* 7(1):7
2. Durão LFCS et al (2016) Distributed manufacturing of spare parts based on additive manufacturing: use cases and technical aspects. *Procedia CIRP* 57:704–709
3. Wittbrodt BT et al (2013) Life-cycle economic analysis of distributed manufacturing with open-source 3-D printers. *Mechatron* 23(6):713–726
4. Berretta S et al (2017) Fused Deposition Modelling of high temperature polymers: exploring CNT PEEK composites. *Polym Test* 63:251–262
5. Rinaldi M et al (2018) Additive layer manufacturing of poly (ether ether ketone) via FDM. *Compos Part B* 145:162–172
6. Geng P et al (2019) Effects of extrusion speed and printing speed on the 3D printing stability of extruded PEEK filament. *J Manuf Process* 37:266–273
7. Zanjanijam AR et al (2020) Fused filament fabrication of peek: a review of process-structure-property relationships. *Polym* 12(8):1665

8. Zhao Y et al (2020) Mechanical characterization of biocompatible PEEK by FDM. *J Manuf Process* 56:28–42
9. Dua R et al (2021) Applications of 3d-printed peek via fused filament fabrication: a systematic review. *Polym* 13(22):4046
10. Fischer M, Schöppner V (2017) Fatigue behavior of FDM parts manufactured with Ultem 9085. *Jom* 69(3):563–568
11. Zaldivar R et al (2017) Influence of processing and orientation print effects on the mechanical and thermal behavior of 3D-Printed ULTEM® 9085 Material. *Addit Manuf* 13:71–80
12. Cicala G et al (2018) Comparison of Ultem 9085 used in fused deposition modelling (FDM) with polyetherimide blends. *Mater* 11(2):285
13. Gebisa AW, Lemu HG (2018) Investigating effects of fused-deposition modeling (FDM) processing parameters on flexural properties of ULTEM 9085 using designed experiment. *Mater* 11(4):500
14. Wu H et al (2018) Multi-functional ULTEM™ 1010 composite filaments for additive manufacturing using fused filament fabrication (FFF). *Addit Manuf* 24:298–306
15. de Bruijn AC, Gómez-Gras G, Pérez MA (2020) Mechanical study on the impact of an effective solvent support-removal methodology for FDM Ultem 9085 parts. *Polym Test* 85:106433
16. McLouth TD et al (2021) Enhancement of FDM ULTEM® 9085 bond strength via atmospheric plasma treatment. *J Manuf Process* 66:179–188
17. Prechtel A et al (2020) Comparison of various 3D printed and milled PAEK materials: effect of printing direction and artificial aging on Martens parameters. *Dent Mater* 36(2):197–209
18. Garcia-Leiner M et al (2021) Characterization of polyaryletherketone (PAEK) filaments and printed parts produced by extrusion-based additive manufacturing. *Polym Int* 70(8):1128–1136
19. Luke SS et al (2021) Effect of fiber content and fiber orientation on mechanical behavior of fused filament fabricated continuous-glass-fiber-reinforced nylon. *Rapid Prototyp J* 27(7):1346–1354
20. Brounstein Z, Yeager CM, Labouriau A (2021) Development of antimicrobial PLA composites for fused filament fabrication. *Polym* 13(4):580
21. Angelopoulos PM, Samouhos M, Taxiarchou M (2021) Functional fillers in composite filaments for fused filament fabrication; a review. *Mater Today:Proc* 37:4031–4043
22. Zhang X, Fan W, Liu T (2020) Fused deposition modeling 3D printing of polyamide-based composites and its applications. *Compos Commun* 21:100413
23. Penumakala PK, Santo J, Thomas A (2020) A critical review on the fused deposition modeling of thermoplastic polymer composites. *Compos Part B* 201:108336
24. Hu C, Qin Q-H (2020) Advances in fused deposition modeling of discontinuous fiber/polymer composites. *Curr Opin Solid State Mater Sci* 24(5):100867
25. Dickson AN, Abourayana HM, Dowling DP (2020) 3D printing of fibre-reinforced thermoplastic composites using fused filament fabrication—a review. *Polym* 12(10):2188
26. Lambiase F, Scipioni SI, Paoletti A (2022) Determination of local density in components made by fused deposition modeling through indentation test. *Int J Adv Manuf Technol* 122(3-4):1467–1478
27. Stamopoulos AG, Scipioni SI, Lambiase F (2023) Experimental characterization of the interlayer fracture toughness of FDM components. *Compos Struct* 320:117213
28. Ko YS et al (2019) Improving the filament weld-strength of fused filament fabrication products through improved interdiffusion. *Addit Manuf* 29:100815
29. Cao D et al (2021) Nanoindentation measurement of core–skin interphase viscoelastic properties in a sandwich glass composite. *Mech Time-Depend Mater* 25:353–363
30. Cao D et al (2022) The effect of resin uptake on the flexural properties of compression molded sandwich composites. *Wind energy* 25(1):71–93
31. Wang X et al (2021) The interfacial shear strength of carbon nanotube sheet modified carbon fiber composites. In: *Challenges in Mechanics of Time Dependent Materials, Volume 2: Proceedings of the 2020 Annual Conference on Experimental and Applied Mechanics*. Springer
32. Yi N et al (2021) Slow and fast crystallising poly aryl ether ketones (PAEKs) in 3D printing: Crystallisation kinetics, morphology, and mechanical properties. *Addit Manuf* 39:101843
33. Lambiase F, Scipioni SI, Paoletti A (2023) Mechanical characterization of FDM parts through instrumented flat indentation. *Int J Adv Manuf Technol* 125(9-10):4201–4211
34. Kumar S, Singh SS, Rozycki P (2022) Numerical simulation of strain-softening behavior of glass-filled polymer composites: comparison of two-dimensional and three-dimensional analyses using Arruda-Boyce and Three-Network viscoplastic models. *Mech Mater* 175:104481
35. Bernard C et al (2017) Numerical implementation of an elastic-viscoplastic constitutive model to simulate the mechanical behaviour of amorphous polymers. *Int J Mater Form* 10:607–621
36. Zhang R et al (2018) Aging-dependent strain localization in amorphous glassy polymers: From necking to shear banding. *Int J Solids Struct* 146:203–213

Publisher's note Springer Nature remains neutral with regard to jurisdictional claims in published maps and institutional affiliations.